

3D Equivariant Visuomotor Policy Learning via Spherical Projection

Boce Hu Dian Wang[†] David Klee Heng Tian Xupeng Zhu Haojie Huang
Robert Platt Robin Walters
Northeastern University
<https://3d-equi-sphere-pro.github.io/>

Abstract

Equivariant models have recently been shown to improve the data efficiency of diffusion policy by a significant margin. However, prior work that explored this direction focused primarily on point cloud inputs generated by multiple cameras fixed in the workspace. This type of point cloud input is not compatible with the now-common setting where the primary input modality is an eye-in-hand RGB camera like a GoPro. This paper closes this gap by incorporating into the diffusion policy model a process that projects features from the 2D RGB camera image onto a sphere. This enables us to reason about symmetries in $SO(3)$ without explicitly reconstructing a point cloud. We perform extensive experiments in both simulation and the real world that demonstrate that our method consistently outperforms strong baselines in terms of both performance and sample efficiency. Our work is the first $SO(3)$ -equivariant policy learning framework for robotic manipulation that works using only monocular RGB inputs.

1 Introduction

The eye-in-hand configuration, where the primary perception modality is a camera mounted near the wrist of the robot, is an important setting for robotic policy learning. This setup avoids the need for carefully calibrated external camera systems, is easier to integrate onto mobile robot platforms, and provides fine-grained visual detail in areas where the robot hand is likely to contact the environment. Moreover, it is used in a growing number of large robot datasets [20, 21, 33, 22, 2].

Unfortunately, there do not yet exist good neural network architectures for leveraging equivariant structure in this setting with only RGB input. Equivariant neural networks improve data efficiency and generalization by incorporating prior knowledge about domain symmetries directly into the model [25, 49, 32]. They have recently been shown to be an effective way of improving data efficiency in diffusion policy [1, 57]. Unfortunately, equivariant diffusion policy works best with point cloud data produced by multiple depth cameras [47]. When used with RGB data, the model ignores the $SO(3)$ structure present in the problem and underperforms the point cloud version significantly [53]. This leaves us with an uncomfortable trade-off – to use an eye-in-hand RGB camera and sacrifice data efficiency or to use a more complex multi-camera point cloud setup.

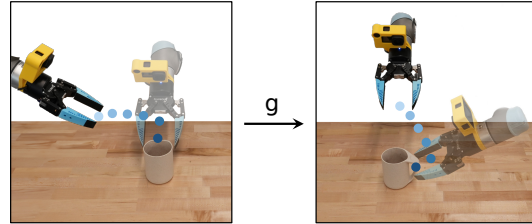


Figure 1: We propose the first $SO(3)$ -equivariant policy learning framework based on a single eye-in-hand RGB image, where the predicted action sequence transforms equivariantly under the same group action $g \in SO(3)$ applied to the scene.

[†] Corresponding to {hu.boce, wang.dian}@northeastern.edu

This paper addresses this challenge by proposing a novel diffusion policy framework that incorporates $SO(3)$ -equivariance into eye-in-hand visuomotor learning. Our method takes only eye-in-hand RGB inputs and projects them onto the sphere. We then rotate the spherical signal to compensate for the motion of the camera. This stable spherical representation enables the network to learn features that transform consistently under 3D rotations and are thus suitable as inputs for equivariant networks. Unlike prior work that relies on segmented point clouds [47, 57] or calibrated multi-camera setups [53], our approach remains equivariant throughout the policy pipeline and supports robust, sample-efficient closed-loop control directly from eye-in-hand inputs. To the best of our knowledge, this is the first framework to learn $SO(3)$ -equivariant visuomotor policies from monocular RGB observations in eye-in-hand settings.

Our key contributions are summarized as follows:

- We propose the first $SO(3)$ -equivariant policy learning framework that uses spherical projection from 2D RGB inputs to model 3D symmetries.
- We theoretically prove that our method achieves global $SO(3)$ -equivariance and local $SO(2)$ -invariance, facilitating policy learning.
- We validate our method through extensive experiments, achieving an average success rate improvement of 11.6% over twelve simulation tasks and 42.5% across four real-world tasks.

2 Related Work

Eye-in-hand Policy Learning Eye-in-hand policy learning [16, 19, 56, 54, 10, 34] has become a flexible and scalable alternative to traditional systems that rely on multiple fixed, externally mounted cameras with precise calibration [53, 47, 58, 5]. By mounting cameras on the robot’s wrist, these methods simplify deployment, avoid explicit calibration, and ease demonstration collection [6, 27, 41, 17]. However, the constantly shifting viewpoint introduces challenges like partial observability, which motivates the use of closed-loop policies that can handle local, viewpoint-dependent observations [59, 17, 4, 37, 60]. Recent work has explored transformer-based [48] or diffusion-based [11] architectures for eye-in-hand-control [61, 10], showing promising results across diverse manipulation tasks. Despite this progress, existing approaches often require large-scale demonstration data [26, 28], and often overlook symmetry structures inherently present in observations. Our method addresses this gap by introducing equivariant representations that encode geometric structure for eye-in-hand settings.

Closed-loop Visuomotor Policy Learning Early approaches to closed-loop visuomotor policy learning relied on reinforcement learning and CNN-based policies to map visual inputs to single-step actions [24, 59, 20]. While effective in simple tasks, these methods were sample-inefficient and struggled to capture multimodal behaviors, as each action was predicted independently without considering temporal context. To address this, subsequent work introduced temporal modeling into behavior cloning frameworks, such as BCRNN [30] and BeT [42], to improve sequential consistency and planning horizons. Building on this direction, recent advances have adopted generative policy models [5, 35, 58, 53], which model multi-step action sequences as a denoising process conditioned on observations. These approaches offer stronger expressiveness and improved multimodal behavior modeling. Our method extends this line of work by further integrating structural inductive biases, enabling more generalizable closed-loop control in complex manipulation settings.

Equivariance in Robotic Manipulation Equivariant and invariant representations have been shown to improve performance and sample efficiency [51, 52, 7, 43, 9, 45]. Prior work has incorporated equivariant architectures for open-loop pick-and-place tasks [63, 13, 14, 8, 36, 40, 50, 15], demonstrating strong performance with fewer demonstrations. Recently, equivariance has been extended to closed-loop diffusion policies [53, 57, 47]. Equivariant Diffusion Policy (EquiDiff) [53] uses an $SO(2)$ -equivariant architecture to enhance Diffusion Policy [5], while EquiBot [57] uses the $SIM(3)$ -equivariant structure with point cloud-based object segmentation. ET-SEED [47] performs trajectory-level $SE(3)$ -equivariant diffusion with simplified conditioning on multi-view point cloud inputs. However, these approaches typically rely on calibrated multi-camera setups or segmented point cloud inputs to model spatial symmetries. Moreover, their architectures are often computationally heavy, limiting their efficiency. These constraints reduce their practicality in eye-in-hand settings, where the continuously shifting viewpoint and monocular RGB input violate the assumptions of existing equivariant models. To address this challenge, we develop a novel diffusion framework that preserves $SO(3)$ -equivariance under eye-in-hand conditions using only RGB observations.

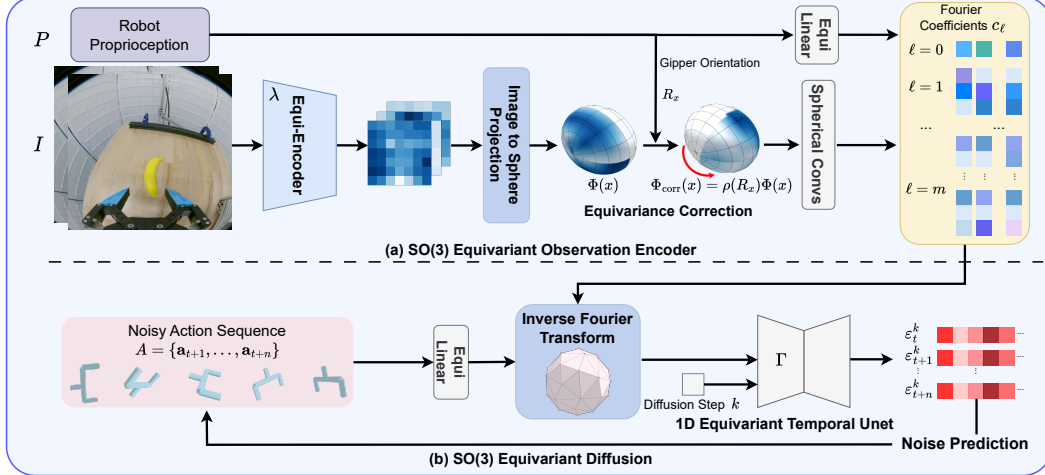


Figure 2: **Overview of our model.** (a) An $\text{SO}(3)$ -equivariant observation encoder extracts features from the RGB input, projects them onto the sphere, and applies an equivariance correction using the gripper orientation R_x to account for the camera’s dynamic viewpoint (red arrow). The corrected spherical signal $\Phi_{\text{corr}}(x)$ is then processed by spherical convolution layers to extract $\text{SO}(3)$ signals. Proprioceptive inputs are embedded via equivariant linear layers. Both image and proprioceptive features are represented as a set of Fourier coefficients c_ℓ on $\text{SO}(3)$ and fused (yellow block). (b) The encoded spherical signals are transformed back to the spatial domain via inverse Fourier transform, sampling finite group elements as the conditioning vector for $\text{SO}(3)$ -equivariant denoising. The noisy action sequence is processed in the same way, through equivariant linear layers and projected onto the same group elements.

3 Background

3.1 Representations of $\text{SO}(3)$

A *group representation* encodes symmetry by mapping elements of a group to linear transformations. In this work, we focus on the special orthogonal group $\text{SO}(3)$ of 3D rotations. A representation of $\text{SO}(3)$ is a homomorphism $\rho : \text{SO}(3) \rightarrow \text{GL}(V)$, where V is a finite-dimensional vector space and $\text{GL}(V)$ denotes the group of invertible linear transformations on V . We highlight three commonly used representations in robotics and geometric deep learning:

- **Degree-0 trivial representation ρ_0 :** Maps every $g \in \text{SO}(3)$ to the identity transformation on \mathbb{R} . This is used for rotation-invariant quantities, such as scalar sensor readings or gripper states.
- **Degree-1 standard representation ρ_1 :** Maps $g \in \text{SO}(3)$ to a 3×3 rotation matrix acting on $v \in \mathbb{R}^3$ via $\rho_1(g)v = gv$, capturing vector features like positions and directions.
- **Higher degree irreducible representations ρ_ℓ :** For $\ell \in \mathbb{N}$, the representation $\rho_\ell : \text{SO}(3) \rightarrow \text{GL}(\mathbb{R}^{2\ell+1})$ is given by the Wigner D -matrix of degree ℓ . It is used to describe higher degree features, such as relative poses, and is often used for latent features in equivariant neural networks.

3.2 Spherical Harmonics and Fourier Coefficients

Spherical harmonics $Y_\ell^m : \mathbb{S}^2 \rightarrow \mathbb{R}$ form an orthonormal basis for square-integrable functions on the 2-sphere and realize the irreducible representations of $\text{SO}(3)$. Any spherical function $\Phi : \mathbb{S}^2 \rightarrow \mathbb{R}^d$ can thus be expanded as:

$$\Phi(\theta, \phi) = \sum_{\ell=0}^{\infty} \sum_{m=-\ell}^{\ell} c_\ell^m Y_\ell^m(\theta, \phi), \quad (1)$$

where c_ℓ^m are the corresponding Fourier coefficients. The mapping $\Phi \mapsto \{c_\ell^m\}$ is known as the Spherical Fourier Transform. Under a rotation $R \in \text{SO}(3)$, each coefficient vector $c_\ell \in \mathbb{R}^{2\ell+1}$ transforms linearly via the representation ρ_ℓ :

$$c'_\ell = \rho_\ell(R) \cdot c_\ell. \quad (2)$$

This enables efficient rotation-equivariant operations on spherical signals in the spectral domain.

3.3 Diffusion Policy

Diffusion-based policy learning [18, 38] is a class of imitation learning methods that model distributions over action trajectories using denoising diffusion probabilistic models (DDPMs) [11]. These methods iteratively denoise sequences of noisy actions, conditioned on observations, to recover expert-like behavior. Formally, given an observation \mathcal{O} and diffusion timestep k , the policy predicts a noise estimate ϵ^k from a corrupted action sequence $\mathbf{a}^k = \mathbf{a}^0 + \epsilon^k$ using a denoiser network Γ . The model is trained to minimize the denoising objective $\mathcal{L}_{\text{diff}} = \mathbb{E}_{\mathbf{a}^0, k, \epsilon^k} [\|\Gamma(\mathcal{O}, \mathbf{a}^k, k) - \epsilon^k\|^2]$. At test time, the policy generates actions by iteratively denoising a randomly initialized sequence from Gaussian noise. Recent extensions [53] incorporate symmetry priors by designing the denoiser to be equivariant with respect to a transformation group G . Specifically, for compact groups such as $\text{SO}(3)$, the denoiser Γ is required to satisfy the equivariance constraint:

$$\Gamma(g \cdot \mathcal{O}, g \cdot \mathbf{a}^k, k) = g \cdot \Gamma(\mathcal{O}, \mathbf{a}^k, k) \quad \forall g \in G. \quad (3)$$

This formulation ensures that the denoising process respects the symmetry of the environment.

3.4 Problem formulation

We study closed-loop robotic visuomotor policy learning through behavior cloning, where a policy is trained to imitate expert demonstrations. Given an observation sequence $\mathcal{O} = \{o_{t-k+1}, \dots, o_t\}$ at timestep t , the learned policy predicts an action chunk $A = \{\mathbf{a}_{t+1}, \dots, \mathbf{a}_{t+n}\}$, where k and n are the observation length and prediction horizon, respectively. Each observation $o = (I, P)$ is comprised of an RGB image I from the wrist-mounted camera, proprioceptive input P describing the end-effector pose. Prior work has shown that higher performance is achieved when using absolute action representations, i.e., actions expressed in the world frame [5, 53]. Following this, we represent each predicted action $a_t \in \mathbb{R}^{10}$ as the absolute end-effector pose including a position in \mathbb{R}^3 , an orientation represented as a 6D rotation vector in \mathbb{R}^6 (see [62]), and a gripper open state in \mathbb{R}^1 . As noted by [53], the absolute action parametrization has a symmetry: 3D transformations of the world frame result in the same 3D transformations to the action. We formalize the equivariance properties of our method in Section 4.1.

4 Method

Figure 2 illustrates an overview of our proposed method, which consists of two key components, an $\text{SO}(3)$ -equivariant observation encoder (Figure 2a) and an $\text{SO}(3)$ -equivariant diffusion module (Figure 2b). The observation encoder uses spherical projection to map image-extracted features onto a hemisphere and applies spherical convolutions to ensure $\text{SO}(3)$ -equivariance, producing the conditioning vector for the diffusion process. The diffusion module is designed as an $\text{SO}(3)$ -equivariant function of the conditioning vectors and noisy inputs. As a result, the entire policy is end-to-end $\text{SO}(3)$ -equivariant. In the following subsections, we first describe our observation encoder, which extracts $\text{SO}(3)$ -equivariant features from 2D images, and then our equivariant diffusion module.

4.1 $\text{SO}(3)$ Equivariant Observation Encoder

This section describes how we construct an $\text{SO}(3)$ -equivariant observation encoder that maps 2D images and robot proprioception into a 3D feature representation. The observation $x \in X$ consists of two parts, an eye-in-hand RGB image I , that captures visual information, and proprioceptive data, $P \in \mathbb{R}^7$, including the end-effector’s 6D pose (position and orientation) and gripper state. Both these signals need to be represented in a way that encodes equivariance. Representing P is relatively easy. Following [53, 57, 40], we embed end-effector pose in $\text{SO}(3)$ using the standard representation and gripper state using the trivial representation (Section 3.1). In contrast, encoding the 2D image input I into $\text{SO}(3)$ -equivariant features is harder because changes in the pose of the wrist-mounted camera induce out-of-plane viewpoint variations that are hard to model. We address this by projecting a standard 2D encoding of the image onto the sphere, as described below and first proposed in the context of object pose estimation [23, 12]. This enables us to reason about $\text{SO}(3)$ action using its irreducible representations encoded as Wigner D-matrices (Section 3.1).

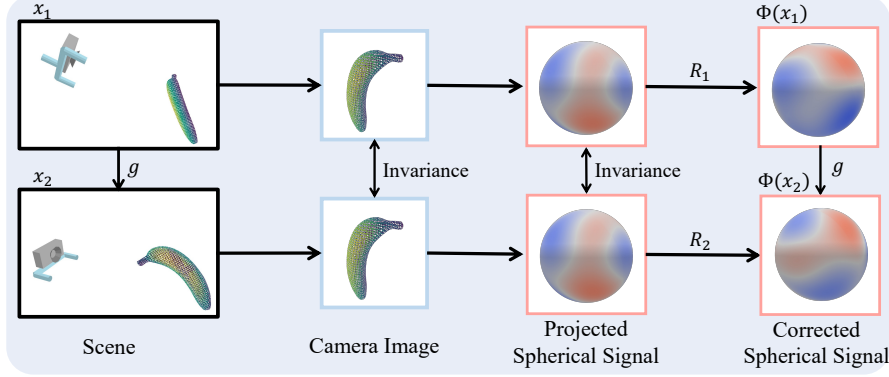


Figure 3: **Illustration of Equivariance Correction.** The left side shows two identical scenes under different global transformations. Since the wrist-mounted camera captures images in its local frame, the resulting images, and thus the projected spherical signals, remain identical across both scenes. By applying the gripper orientation R as an equivariance correction, we align these spherical signals to a common world frame, ensuring their equivariant transformation under global scene rotations.

Image Encoder Our image encoder is detailed in Figure 2a. First, we encode the input image I from the observation x using a standard $\text{SO}(2)$ -equivariant image encoder λ (i.e. Equivariant ResNet-18). Next, the resulting feature map, $\lambda(I)$, is mapped onto the sphere using an orthographic projection. This converts a “flat” image into a spherical signal $\Phi(x) : \mathbb{S}^2 \rightarrow \mathbb{R}^d$ that is easier to manipulate in $\text{SO}(3)$. We represent this spherical signal in the spectral domain as truncated Fourier coefficients calculated using the spherical Fourier transform (Equation 1).

Equivariance Correction At this point, the image encoding has been projected onto the sphere and represented using spherical harmonics. However, there is a problem. Since global 3D transformations of the world transform the camera and objects equally, the observed image and the projected signal $\Phi(x)$ would be invariant. This introduces a mismatch in that $\Phi(x)$ stays constant while the world and actions rotate, thereby breaking global $\text{SO}(3)$ -equivariance. We accommodate this by rotating the spherical signal by an amount corresponding to the $\text{SO}(3)$ orientation of the gripper. We call this the *equivariance correction* factor, and it is illustrated in Figure 3. On the left of Figure 3, we see two scenes that are the same except for an $\text{SO}(3)$ rotation of g . The eye-in-hand camera image (of the banana) is the same in both situations, even though the scene is rotated. This results in the identical projected spherical signal. It is only by applying the equivariance correction factor to the two respective signals (R_1 and R_2) that we recover the camera pose in the spherical signal. This ensures that the spherical signals produced in different camera poses are represented in a consistent global frame. We analyze this approach below.

Definition 1 (Equivariance Correction). *Let G be a group acting on the input space X and output space Y . For a function $f : X \rightarrow Y$, an Equivariance-Correction map is any $\mathcal{C} : X \rightarrow G$ satisfying $\mathcal{C}(g \cdot x) f(g \cdot x) = g \mathcal{C}(x) f(x)$ for all $g \in G$, and $x \in X$. The corrected function $f_{\text{corr}}(x) = \mathcal{C}(x) f(x)$ is therefore G -equivariant.*

Notice that Definition 1 implies $f(x)$ and $f(gx)$ are in the same orbit. Equivariance Correction is similar to a *canonicalization map* $c : X \rightarrow G$, where $f_{\text{cano}} = c(x)f(c(x)^{-1}x)$ transforms the input to a canonical frame then transforms the output back to the original frame. When $f(x) = f(gx)$, Equivariance Correction is a special case of canonicalization where $f(c(x)^{-1}x) = f(x)$ is invariant, so it only transforms the output to restore equivariance without altering the input.

We now show that Definition 1 is satisfied when the correction map is chosen to be the end-effector rotation. Let $x \in X$ denote the robot observation at a given timestep, which includes an eye-in-hand RGB image I and the corresponding camera (end-effector) pose $R_x \in \text{SO}(3)$ in the world frame. Let $\Phi(x)$ denote the spherical signal derived from the image I , expressed in the camera frame, and let ρ be a representation of $\text{SO}(3)$ acting on $\Phi(x)$.

Proposition 1 (Equivariance Correction via End-Effector Pose). *The map $\mathcal{C} : (I, R_x) \mapsto R_x$, which assigns each camera image to its corresponding camera pose $R_x \in \text{SO}(3)$ is an equivariance correction. The corrected signal $\Phi_{\text{corr}}(x) = \rho(\mathcal{C}(x))\Phi(x) = \rho(R_x)\Phi(x)$ is in a world-aligned frame. Thus, the mapping Φ_{corr} is $\text{SO}(3)$ -equivariant: for any global rotation $g \in \text{SO}(3)$, we have $\Phi_{\text{corr}}(g \cdot x) = \rho(g)\Phi_{\text{corr}}(x)$.*

Proof. Let $g \in \text{SO}(3)$ be a global rotation applied simultaneously to the scene and the camera. Because the image is recorded in the camera frame, the spherical signal is unaffected, i.e. $\Phi(g \cdot x) = \Phi(x)$, while the camera pose updates as $R_x \mapsto R_{gx} = gR_x$. For the corrected signal, we therefore obtain

$$\Phi_{\text{corr}}(gx) = \rho(R_{gx})\Phi(gx) = \rho(g)\rho(R_x)\Phi(x) = \rho(g)\Phi_{\text{corr}}(x), \quad (4)$$

where the second equality follows from the homomorphism property $\rho(gR_x) = \rho(g)\rho(R_x)$ of the representation ρ . Hence the map Φ_{corr} is $\text{SO}(3)$ -equivariant. \square

A concrete realization of ρ with the spherical-harmonic coefficients and Wigner D -matrices is given in Appendix A, where the proposition reduces to the rotation of coefficient vectors in Eq. 2.

Camera-rotation invariance. Our model also enforces an additional symmetry, rotations of the camera around its optical axis while the object remains stationary. These rotations form an $\text{SO}(2)$ subgroup. Such rotations transform both the image and the camera pose, but their effects cancel out in the corrected world-frame signal. We now formalize the invariance of the corrected world-frame signal under such transformations.

Proposition 2 (Invariance to $\text{SO}(2)$ Rotation of the Eye-in-hand Camera). *Let $g \in \text{SO}(2)$ be a rotation about the camera’s optical axis. Then, under the transformation $(I, R_x) \mapsto (g \cdot I, R_x g^{-1})$, the corrected signal defined in Proposition 1 remains invariant: $\Phi_{\text{corr}}(g \cdot x) = \Phi_{\text{corr}}(x)$.*

Proof. Assume the image encoder λ is $\text{SO}(2)$ -equivariant, i.e., $\lambda(g \cdot I) = g \cdot \lambda(I)$ for all $g \in \text{SO}(2)$. Because spherical projection and spherical Fourier transform preserve equivariance, the spherical signal satisfies $\Phi(g \cdot x) = g \cdot \Phi(x)$. Meanwhile, the camera pose transforms as $R_x \mapsto R_x g^{-1}$, since applying an $\text{SO}(2)$ rotation g in the camera (eye-in-hand) frame corresponds to a right multiplication by g^{-1} on its world-frame orientation R_x (i.e., rotating the camera relative to itself). The corrected signal is:

$$\Phi_{\text{corr}}(g \cdot x) = \rho(R_x g^{-1}) \Phi(g \cdot x) = \rho(R_x g^{-1}) \rho(g) \Phi(x) = \rho(R_x) \Phi(x) = \Phi_{\text{corr}}(x). \quad (5)$$

Thus, the corrected signal is invariant under any $\text{SO}(2)$ rotations of the eye-in-hand camera. \square

By combining Propositions 1 and 2, we obtain a two-level symmetry in the encoder: the features are globally $\text{SO}(3)$ -equivariant and locally $\text{SO}(2)$ -invariant to rotations of the camera around its optical axis. These properties are inherently preserved without requiring additional constraints. As shown in Section 5, encoding these properties into the network leads to empirically improved performance.

4.2 $\text{SO}(3)$ Equivariant Diffusion

As described in Section 3.3, we enforce end-to-end $\text{SO}(3)$ -equivariance by requiring the denoising network Γ to satisfy: $\Gamma(g \cdot \mathcal{O}, g \cdot \mathbf{a}^k, k) = g \cdot \Gamma(\mathcal{O}, \mathbf{a}^k, k)$ for all $g \in \text{SO}(3)$. To achieve this, we extend the 2D denoising model from *EquiDiff* [53] to 3D. *EquiDiff* applies a shared 1D temporal U-Net independently to each group element in $C_n \subset \text{SO}(2)$. This element-wise weight sharing guarantees that the same parameters act on every group element, resulting in a noise embedding in the regular representation.

To generalize to 3D, we approximate the continuous symmetry group $\text{SO}(3)$ with a finite subgroup and perform sampling accordingly. Denote $H \subset \text{SO}(3)$ the subgroup that the diffusion process is equivariant to (e.g., the icosahedral group I_{60}). Denote $S \subset \text{SO}(3)$ a set that is closed under H , i.e., $HS = S$. Intuitively, S could be viewed as copies of the rotations in H , each with different offset angles to capture a denser discrete signal. Given a signal $\Psi : \text{SO}(3) \rightarrow \mathbb{R}^d$, we first sample $\Psi(S) = \{\Psi(s_i) : s_i \in S\}$ and then evaluate the U-Net pointwise on each sample $\Gamma(\Psi(S)) = \{\Gamma(\Psi(s_i)) : s_i \in S\}$, where both the input and output can be treated as copies of the regular representations of H . Since $g \in H$ permutes the order of $\Psi(S)$ and $\Gamma(\Psi(S))$ identically, the entire process is H -equivariant. Because the spherical convolution layers output a signal on $\text{SO}(3)$, we can flexibly choose any finite group H and sampling set S for discretization. In our implementation, we use both $C_8 \subset \text{SO}(2)$ and $I_{60} \subset \text{SO}(3)$ as choices of H . We refer readers to Appendix B for further details.



Figure 5: A subset of experimental environments from MimicGen [31]. Left: external view of the task. Right: eye-in-hand observation used by our method. The full set of tasks is shown in Appendix C.

4.3 End-to-End Symmetry Analysis

In this section, we analyze the equivariant properties of our method. First, combining the $SO(3)$ -equivariant encoder (Proposition 1) and the $SO(3)$ -equivariant diffusion (Section 4.2), our policy maintains end-to-end symmetry to global scene $SO(3)$ rotations, which would significantly improve its sample efficiency and generalizability to world coordinate frame changes. The benefit of the $SO(2)$ invariance from the image encoder (Proposition 2) is subtle. Under a relative rotation of the gripper with respect to the workspace, no a priori constraint can be placed on how the action trajectory should transform; however, the diffusion model is provided with a hybrid invariant (from the image encoder) and equivariant (from the proprioceptive information) feature, helping it to learn a fused invariant-equivariant action. In particular, the image features and the proprioceptive features have been transformed to the same frame as the output actions. Figure 4 illustrates this benefit. In both states (a) and (b), the gripper (triangle) is trying to reach the same goal pose (star), but the gripper in (b) is rotated by 90° around its optical axis. Translationally, the action should remain invariant (red dots), while rotationally, the action needs to gradually transform from an equivariant (yellow) to an invariant (green) behavior. The hybrid invariant-equivariant feature in our model provides a rich geometric structure for learning such trajectories, whereas non-equivariant models must infer such patterns from data alone. This advantage is empirically validated in Section 5.

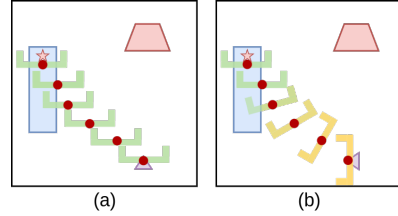


Figure 4: Illustration of translation invariance and rotation equivariance-to-invariance transition.

5 Experiments

5.1 Simulation

Experiment Setting We evaluate our method on twelve robotic manipulation tasks from the MimicGen benchmark [31], which is widely used in previous work on closed-loop policy learning [7, 53]. A representative subset of these simulation tasks is shown in Figure 5 (see Appendix C for a full description of all twelve MimicGen tasks). Policies are trained and evaluated exclusively using eye-in-hand RGB observations (right image in each subfigure of Figure 5). To capture sufficient scene context, we enlarge the camera’s field of view (FOV) to approximate a typical GoPro setup and re-generate the enlarged FOV observations using the original Mimicgen demonstration data for our method and baselines. Each model is trained with 100 and 200 demonstrations, and evaluated with 50 rollouts per task with 3 random seeds. Task and training details are provided in Appendix C and D.

Baselines Our experiments aim to validate the benefits of explicitly modeling equivariance in eye-in-hand visuomotor policies. We evaluate two versions of our method with different symmetry levels, an $SO(3)$ -equivariant version and an $SO(2)$ -equivariant variant which is symmetric only about rotations in the plane of the table. Although the $SO(3)$ version has more symmetry, the $SO(2)$ version is more lightweight, which may be preferable in some settings. We compare against three strong baselines: (1) **Diffusion Policy** [5]: A diffusion-based policy without any equivariance, serving as the primary reference. (2) **EquiDiff (modified)** [53]: Designed for fixed-camera settings, it achieves $SO(2)$ equivariance via an equivariant image encoder and an equivariant temporal U-Net. For eye-in-hand control, we replace its image encoder with a standard ResNet, so only proprioception and denoising remain equivariant. (3) **ACT** [61]: A transformer-based behavior cloning method. To ensure a fair comparison, all experiments in the following sections, including ablations and method variants, consistently **apply** $SO(2)$ data augmentation during training by rotating the end-effector pose in both proprioception and actions, equivalent to jointly rotating the gripper and scene.

Table 1: Success rates (%) on MimicGen tasks with 100 and 200 demos, averaged over 3 seeds. We report both the mean performance across all tasks and per-task results. The best performance is shown in **bold**, and the second best is underlined. Full results with standard deviations are in Appendix E.

Method	Mean		Stack D1		Stack Three D1		Square D2		Threading D0		Three Pc. D0		Hammer Cl. D1	
	100	200	100	200	100	200	100	200	100	200	100	200	100	200
Ours(SO(3))	65.2 (+11.6)	75.0 (+10.5)	99	100	70	88	35	51	90	92	71	79	66	73
Ours(SO(2))	65.0 (+11.4)	73.1 (+8.6)	98	100	75	88	32	51	85	87	75	80	71	73
DiffPo	53.6	64.1	91	96	43	77	12	25	77	87	73	73	59	63
EquiDiff	53.0	64.5	96	99	61	80	9	19	89	92	74	79	59	74
ACT	23	40.9	45	77	12	37	3	10	36	53	28	50	35	63

Method	Mug Cl. D1		Coffee D2		Kitchen D1		Pick Place D0		Coffee Prep. D1		Nut Asse. D0		
	100	200	100	200	100	200	100	200	100	200	100	200	
Ours(SO(3))		54	59	64	69	75	79	42	66	41	61	75	82
Ours(SO(2))		56	61	59	63	65	72	46	61	47	56	74	84
DiffPo		49	61	53	55	61	71	36	48	37	52	51	62
EquiDiff		51	62	47	61	55	67	28	46	27	39	40	56
ACT		25	37	21	35	21	51	9	14	8	16	37	49

Results Table 1 reports the maximum success rates across all methods and configurations. In terms of performance, our SO(3)-equivariant model achieves the best results in 21 out of 24 task settings, consistently outperforming the baselines. The remaining three settings show only marginal differences (within 1-2%), all within the standard error margins. Similarly, our SO(2)-equivariant variant outperforms baselines in 20 settings, which further validates the effectiveness of our design. With only 100 demos, our model exceeds the best-performing baseline by an average of 11.6%. With 200 demons, the advantage remains similar at 10.5%. Importantly, our model trained with 100 demos surpasses all baselines trained with 200 demos and additional data augmentation, clearly demonstrating superior data efficiency. These results collectively highlight that the explicit modeling of equivariance is the key factor driving both the improved performance and enhanced sample efficiency of our method. Appendix E provides the full experimental results with standard deviations across three random seeds. Additionally, we evaluate the benefits of pretraining equivariant image encoders, with results provided in Appendix F.

Ablation Study To assess the contribution of each component of our method, we conduct an ablation study on four representative tasks with 100 demos: Stack Three D1, Square D2, Coffee D2, and Nut assembly D0. We evaluate the following variants of our SO(3)-equivariant version, each corresponding to a core module in our design: (1) **Sphere**: With or without the spherical projection and spherical convolutions for extracting SO(3)-equivariant features from images. (2) **EquiEnc**: With or without the proposed equivariant image encoder that captures SO(2)-invariant features (Proposition 2). (3) **EquiU**: With or without an equivariant temporal denoising U-Net in the diffusion module. The results are summarized in Table 2. Removing the spherical projection leads to the largest performance drop of 9.2%, highlighting its critical role in capturing symmetries, despite the use of data augmentation. Disabling the equivariant image encoder and the equivariant U-Net results in drops of 6.8% and 6.7%, respectively. These results demonstrate that all three components—spherical lifting, invariant encoding, and equivariant denoising—are essential for the overall effectiveness of our method.

Table 2: Ablation study results. A red cross indicates that the corresponding module is removed in that variant.

Sphere	EquiEnc	EquiU	Sta.	Cof.	Nut.	Squ.	Mean
✗	✓	✓	63.3	61.3	59.0	23.3	51.8 (-9.2)
✓	✗	✓	66.0	57.3	61.3	32.0	54.2 (-6.8)
✓	✓	✗	68.7	58.7	58.0	32.0	54.3 (-6.7)
✓	✓	✓	70.0	64.0	75.3	34.7	61.0

5.2 Real World

Physical Setups Our real robot experiments use a Universal Robot UR5 equipped with a Robotiq-85 Gripper and custom-designed soft fingers. A GoPro camera is mounted on the wrist, following prior setups [6, 10, 26]. Demonstrations are collected via the Gello teleoperation interface [55], with observations and actions recorded at 5 Hz. Following [5, 53], we employ DDIM [44] to reduce the number of denoising steps to 16. Figure 6 illustrates the four real-world manipulation tasks. The first

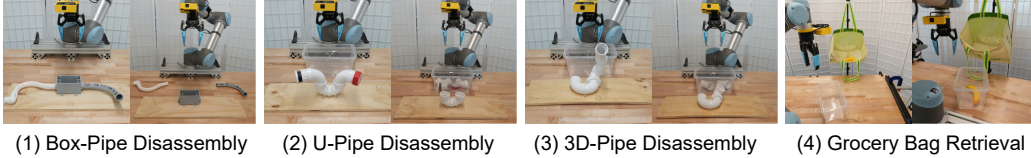


Figure 6: Real-world environments for evaluation. A GoPro camera is mounted on the robot’s wrist to capture eye-in-hand observations. In each subfigure, the left image shows the initial state, while the right image shows the goal state. See Appendix G for detailed task descriptions.

three tasks involve pipe disassembly, each focusing on different challenges in closed-loop control: background-object segmentation (Box-Pipe), long-horizon control (U-Pipe), and handling complex 3D geometries (3D-Pipe). The fourth task involves retrieving objects from a deformable grocery bag, which relies on wrist-mounted camera observations due to occlusions and limited external visibility. We compare our method (the $SO(3)$ version) against the Diffusion Policy [5]. Further details on the physical setup, task visualization, and goal specification are provided in Appendix G.

Results Table 3 reports success rates over 20 trials per task. Our method consistently outperforms the Diffusion Policy [5] baseline, with significant improvements on Box-Pipe (80% vs. 10%) and 3D-Pipe (75% vs. 15%). The former benefits from more precise visual representations that distinguish the gray pipe from the gray box background,

while the latter showcases the advantage of $SO(3)$ -equivariant features for reasoning over complex 3D geometries. The U-Pipe task also shows a notable gain (85% vs. 65%), demonstrating the sustained and stable performance of our equivariant method in the long-horizon task. On the Grocery Bag task, which heavily relies on eye-in-hand perception, our method achieves 95% success rate, further highlighting its robustness in unstructured environments. These results confirm the effectiveness of our equivariant design in addressing diverse manipulation challenges in the real world. See Appendix H for more details of failure analysis.

Table 3: Real-world task success rates over 20 trials. The number of demonstrations used for training each task is shown in the second row.

	Box-Pipe	U-Pipe	3D-Pipe	Grocery Bag
# Demos	65	65	65	60
Ours	80%(16/20)	85%(17/20)	75%(15/20)	95%(19/20)
DiffPo [5]	10%(2/20)	65%(13/20)	15%(3/20)	75%(15/20)

6 Conclusion

In this paper, we propose the first $SO(3)$ -equivariant policy learning framework for eye-in-hand visuomotor control using only monocular RGB inputs. By lifting 2D image features onto the sphere and introducing an equivariance correction mechanism to compensate for dynamic camera viewpoints, our method achieves global $SO(3)$ -equivariance and local $SO(2)$ -invariance without relying on depth sensors or multi-camera setups. This design enables robust and sample-efficient policy learning in dynamic, real-world settings. Extensive experiments in both simulation and real-world tasks demonstrate that our method consistently outperforms strong baselines, achieving higher success rates with fewer demonstrations. Our work provides a general and effective algorithmic solution that is both deployable and scalable for eye-in-hand visuomotor learning.

Limitations Our method has several limitations for future investigation. First, we only consider a single wrist-mounted RGB camera. While this view provides fine-grained local information, it lacks global scene context that an agent-view camera could offer. Effectively combining these complementary perspectives remains an important challenge. Second, our approach models rotational equivariance but does not address translational equivariance. This limits the model’s ability to generalize to object translations within the scene. Extending the equivariance correction to handle camera translations is a promising direction for future work. Third, the use of equivariant networks increases training time. Although inference remains efficient, reducing training overhead through more lightweight architectures would further enhance practicality. Fourth, our current method focuses on single-arm manipulation. Extending the framework to bimanual systems, where coordination between two arms is required, is a natural next step. Finally, our method does not yet leverage vision-language models. Integrating high-level semantic understanding through vision language models could further improve generalization and task understanding in more diverse environments.

References

- [1] Johann Brehmer, Joey Bose, Pim De Haan, and Taco Cohen. EDGI: Equivariant Diffusion for Planning with Embodied Agents. *arXiv preprint arXiv:2303.12410*, 2023.
- [2] Anthony Brohan, Noah Brown, Justice Carbajal, Yevgen Chebotar, Joseph Dabis, Chelsea Finn, Keerthana Gopalakrishnan, Karol Hausman, Alex Herzog, Jasmine Hsu, et al. Rt-1: Robotics transformer for real-world control at scale. *arXiv preprint arXiv:2212.06817*, 2022.
- [3] Gabriele Cesa, Leon Lang, and Maurice Weiler. A program to build E(N)-equivariant steerable CNNs. In *International Conference on Learning Representations*, 2022. URL <https://openreview.net/forum?id=WE4qe9xlnQw>.
- [4] Ricson Cheng, Arpit Agarwal, and Katerina Fragkiadaki. Reinforcement learning of active vision for manipulating objects under occlusions. In *Conference on robot learning*, pages 422–431. PMLR, 2018.
- [5] Cheng Chi, Zhenjia Xu, Siyuan Feng, Eric Cousineau, Yilun Du, Benjamin Burchfiel, Russ Tedrake, and Shuran Song. Diffusion policy: Visuomotor policy learning via action diffusion. *The International Journal of Robotics Research*, page 02783649241273668, 2023.
- [6] Cheng Chi, Zhenjia Xu, Chuer Pan, Eric Cousineau, Benjamin Burchfiel, Siyuan Feng, Russ Tedrake, and Shuran Song. Universal manipulation interface: In-the-wild robot teaching without in-the-wild robots. *arXiv preprint arXiv:2402.10329*, 2024.
- [7] Niklas Funk, Julen Urain, Joao Carvalho, Vignesh Prasad, Georgia Chalvatzaki, and Jan Peters. Actionflow: Equivariant, accurate, and efficient policies with spatially symmetric flow matching. *arXiv preprint arXiv:2409.04576*, 2024.
- [8] Chongkai Gao, Zhengrong Xue, Shuying Deng, Tianhai Liang, Siqi Yang, Lin Shao, and Huazhe Xu. Riemann: Near real-time se(3)-equivariant robot manipulation without point cloud segmentation. *arXiv preprint arXiv:2403.19460*, 2024.
- [9] Jiaqi Guan, Wesley Wei Qian, Xingang Peng, Yufeng Su, Jian Peng, and Jianzhu Ma. 3D Equivariant Diffusion for Target-Aware Molecule Generation and Affinity Prediction. In *The Eleventh International Conference on Learning Representations*, 2023.
- [10] Huy Ha, Yihuai Gao, Zipeng Fu, Jie Tan, and Shuran Song. Umi on legs: Making manipulation policies mobile with manipulation-centric whole-body controllers. *arXiv preprint arXiv:2407.10353*, 2024.
- [11] Jonathan Ho, Ajay Jain, and Pieter Abbeel. Denoising diffusion probabilistic models. *Advances in neural information processing systems*, 33:6840–6851, 2020.
- [12] Owen Howell, David Klee, Ondrej Biza, Linfeng Zhao, and Robin Walters. Equivariant single view pose prediction via induced and restriction representations. *Advances in Neural Information Processing Systems*, 36:47251–47263, 2023.
- [13] Boce Hu, Xupeng Zhu, Dian Wang, Zihao Dong, Haojie Huang, Chenghao Wang, Robin Walters, and Robert Platt. Orbitgrasp: $SE(3)$ -equivariant grasp learning. *arXiv preprint arXiv:2407.03531*, 2024.
- [14] Haojie Huang, Dian Wang, Robin Walters, and Robert Platt. Equivariant transporter network. *arXiv preprint arXiv:2202.09400*, 2022.
- [15] Haojie Huang, Dian Wang, Arsh Tangri, Robin Walters, and Robert Platt. Leveraging symmetries in pick and place. *The International Journal of Robotics Research*, 43(4):550–571, 2024.
- [16] Physical Intelligence, Kevin Black, Noah Brown, James Darpinian, Karan Dhabalia, Danny Driess, Adnan Esmail, Michael Equi, Chelsea Finn, Niccolo Fusai, et al. $\pi_{0.5}$: A vision-language-action model with open-world generalization. *arXiv preprint arXiv:2504.16054*, 2025.

- [17] Rishabh Jangir, Nicklas Hansen, Sambaran Ghosal, Mohit Jain, and Xiaolong Wang. Look closer: Bridging egocentric and third-person views with transformers for robotic manipulation. *IEEE Robotics and Automation Letters*, 7(2):3046–3053, 2022.
- [18] Michael Janner, Yilun Du, Joshua Tenenbaum, and Sergey Levine. Planning with Diffusion for Flexible Behavior Synthesis. In *International Conference on Machine Learning*, pages 9902–9915. PMLR, 2022.
- [19] Yunfan Jiang, Ruohan Zhang, Josiah Wong, Chen Wang, Yanjie Ze, Hang Yin, Cem Gokmen, Shuran Song, Jiajun Wu, and Li Fei-Fei. Behavior robot suite: Streamlining real-world whole-body manipulation for everyday household activities. *arXiv preprint arXiv:2503.05652*, 2025.
- [20] Dmitry Kalashnikov, Alex Irpan, Peter Pastor, Julian Ibarz, Alexander Herzog, Eric Jang, Deirdre Quillen, Ethan Holly, Mrinal Kalakrishnan, Vincent Vanhoucke, et al. Scalable deep reinforcement learning for vision-based robotic manipulation. In *Conference on robot learning*, pages 651–673. PMLR, 2018.
- [21] Dmitry Kalashnikov, Jacob Varley, Yevgen Chebotar, Benjamin Swanson, Rico Jonschkowski, Chelsea Finn, Sergey Levine, and Karol Hausman. Mt-opt: Continuous multi-task robotic reinforcement learning at scale. *arXiv preprint arXiv:2104.08212*, 2021.
- [22] Alexander Khazatsky, Karl Pertsch, Suraj Nair, Ashwin Balakrishna, Sudeep Dasari, Siddharth Karamcheti, Soroush Nasiriany, Mohan Kumar Srirama, Lawrence Yunliang Chen, Kirsty Ellis, et al. Droid: A large-scale in-the-wild robot manipulation dataset. *arXiv preprint arXiv:2403.12945*, 2024.
- [23] David M Klee, Ondrej Biza, Robert Platt, and Robin Walters. Image to sphere: Learning equivariant features for efficient pose prediction. *arXiv preprint arXiv:2302.13926*, 2023.
- [24] Sergey Levine, Chelsea Finn, Trevor Darrell, and Pieter Abbeel. End-to-end training of deep visuomotor policies. *Journal of Machine Learning Research*, 17(39):1–40, 2016.
- [25] Yi-Lun Liao and Tess Smidt. Equiformer: Equivariant graph attention transformer for 3d atomistic graphs. In *The Eleventh International Conference on Learning Representations*, 2023. URL <https://openreview.net/forum?id=KwmPfARg0TD>.
- [26] Fanqi Lin, Yingdong Hu, Pingyue Sheng, Chuan Wen, Jiacheng You, and Yang Gao. Data scaling laws in imitation learning for robotic manipulation. *arXiv preprint arXiv:2410.18647*, 2024.
- [27] Kehui Liu, Chuyue Guan, Zhongjie Jia, Ziniu Wu, Xin Liu, Tianyu Wang, Shuai Liang, Peng Chen, Pingrui Zhang, Haoming Song, et al. Fastumi: A scalable and hardware-independent universal manipulation interface with dataset. *arXiv e-prints*, pages arXiv–2409, 2024.
- [28] Songming Liu, Lingxuan Wu, Bangguo Li, Hengkai Tan, Huayu Chen, Zhengyi Wang, Ke Xu, Hang Su, and Jun Zhu. Rdt-1b: a diffusion foundation model for bimanual manipulation. *arXiv preprint arXiv:2410.07864*, 2024.
- [29] Ilya Loshchilov and Frank Hutter. Decoupled weight decay regularization. *arXiv preprint arXiv:1711.05101*, 2017.
- [30] Ajay Mandlekar, Danfei Xu, Josiah Wong, Soroush Nasiriany, Chen Wang, Rohun Kulkarni, Li Fei-Fei, Silvio Savarese, Yuke Zhu, and Roberto Martín-Martín. What matters in learning from offline human demonstrations for robot manipulation. *arXiv preprint arXiv:2108.03298*, 2021.
- [31] Ajay Mandlekar, Soroush Nasiriany, Bowen Wen, Ireteayo Akinola, Yashraj Narang, Linxi Fan, Yuke Zhu, and Dieter Fox. Mimicgen: A data generation system for scalable robot learning using human demonstrations. *arXiv preprint arXiv:2310.17596*, 2023.
- [32] Arnab Kumar Mondal, Pratheeksha Nair, and Kaleem Siddiqi. Group equivariant deep reinforcement learning. *arXiv preprint arXiv:2007.03437*, 2020.

- [33] Abby O’Neill, Abdul Rehman, Abhiram Maddukuri, Abhishek Gupta, Abhishek Padalkar, Abraham Lee, Acorn Pooley, Agrim Gupta, Ajay Mandlekar, Ajinkya Jain, et al. Open x-embodiment: Robotic learning datasets and rt-x models: Open x-embodiment collaboration 0. In *2024 IEEE International Conference on Robotics and Automation (ICRA)*, pages 6892–6903. IEEE, 2024.
- [34] Karl Pertsch, Kyle Stachowicz, Brian Ichter, Danny Driess, Suraj Nair, Quan Vuong, Oier Mees, Chelsea Finn, and Sergey Levine. Fast: Efficient action tokenization for vision-language-action models. *arXiv preprint arXiv:2501.09747*, 2025.
- [35] Aaditya Prasad, Kevin Lin, Jimmy Wu, Linqi Zhou, and Jeannette Bohg. Consistency policy: Accelerated visuomotor policies via consistency distillation. *arXiv preprint arXiv:2405.07503*, 2024.
- [36] Yu Qi, Yuanchen Ju, Tianming Wei, Chi Chu, Lawson LS Wong, and Huazhe Xu. Two by two: Learning multi-task pairwise objects assembly for generalizable robot manipulation. *CVPR 2025*, 2025.
- [37] Allen Z Ren, Justin Lidard, Lars L Ankile, Anthony Simeonov, Pulkit Agrawal, Anirudha Majumdar, Benjamin Burchfiel, Hongkai Dai, and Max Simchowitz. Diffusion policy policy optimization. *arXiv preprint arXiv:2409.00588*, 2024.
- [38] Moritz Reuss, Maximilian Li, Xiaogang Jia, and Rudolf Lioutikov. Goal conditioned imitation learning using score-based diffusion policies. In *Robotics: Science and Systems*, 2023.
- [39] Olga Russakovsky, Jia Deng, Hao Su, Jonathan Krause, Sanjeev Satheesh, Sean Ma, Zhiheng Huang, Andrej Karpathy, Aditya Khosla, Michael Bernstein, et al. Imagenet large scale visual recognition challenge. *International journal of computer vision*, 115:211–252, 2015.
- [40] Hyunwoo Ryu, Jiwoo Kim, Hyunseok An, Junwoo Chang, Joohwan Seo, Taehan Kim, Yubin Kim, Chaewon Hwang, Jongeun Choi, and Roberto Horowitz. Diffusion-edfs: Bi-equivariant denoising generative modeling on se (3) for visual robotic manipulation. In *Proceedings of the IEEE/CVF Conference on Computer Vision and Pattern Recognition*, pages 18007–18018, 2024.
- [41] Mingyo Seo, H. Andy Park, Shenli Yuan, Yuke Zhu, , and Luis Sentis. Legato: Cross-embodiment imitation using a grasping tool. *IEEE Robotics and Automation Letters (RA-L)*, 2025.
- [42] Nur Muhammad Shafiullah, Zichen Cui, Ariuntuya Arty Altanzaya, and Lerrel Pinto. Behavior transformers: Cloning k modes with one stone. *Advances in neural information processing systems*, 35:22955–22968, 2022.
- [43] Anthony Simeonov, Yilun Du, Andrea Tagliasacchi, Joshua B Tenenbaum, Alberto Rodriguez, Pulkit Agrawal, and Vincent Sitzmann. Neural descriptor fields: Se (3)-equivariant object representations for manipulation. In *2022 International Conference on Robotics and Automation (ICRA)*, pages 6394–6400. IEEE, 2022.
- [44] Jiaming Song, Chenlin Meng, and Stefano Ermon. Denoising diffusion implicit models. *arXiv preprint arXiv:2010.02502*, 2020.
- [45] Sangli Teng, William Clark, Anthony Bloch, Ram Vasudevan, and Maani Ghaffari. Lie algebraic cost function design for control on lie groups. In *2022 IEEE 61st Conference on Decision and Control (CDC)*, pages 1867–1874. IEEE, 2022.
- [46] Nathaniel Thomas, Tess Smidt, Steven Kearnes, Lusann Yang, Li Li, Kai Kohlhoff, and Patrick Riley. Tensor field networks: Rotation-and translation-equivariant neural networks for 3d point clouds. *arXiv preprint arXiv:1802.08219*, 2018.
- [47] Chenrui Tie, Yue Chen, Ruihai Wu, Boxuan Dong, Zeyi Li, Chongkai Gao, and Hao Dong. Et-seed: Efficient trajectory-level se (3) equivariant diffusion policy. *arXiv preprint arXiv:2411.03990*, 2024.

- [48] Ashish Vaswani, Noam Shazeer, Niki Parmar, Jakob Uszkoreit, Llion Jones, Aidan N Gomez, Łukasz Kaiser, and Illia Polosukhin. Attention is all you need. *Advances in neural information processing systems*, 30, 2017.
- [49] Robin Walters, Jinxi Li, and Rose Yu. Trajectory prediction using equivariant continuous convolution. *arXiv preprint arXiv:2010.11344*, 2020.
- [50] Dian Wang, Mingxi Jia, Xupeng Zhu, Robin Walters, and Robert Platt. On-robot learning with equivariant models. *arXiv preprint arXiv:2203.04923*, 2022.
- [51] Dian Wang, Robin Walters, and Robert Platt. $so(2)$ -equivariant reinforcement learning. *arXiv preprint arXiv:2203.04439*, 2022.
- [52] Dian Wang, Robin Walters, Xupeng Zhu, and Robert Platt. Equivariant q learning in spatial action spaces. In *Conference on Robot Learning*, pages 1713–1723. PMLR, 2022.
- [53] Dian Wang, Stephen Hart, David Surovik, Tarik Kelestemur, Haojie Huang, Haibo Zhao, Mark Yeatman, Jiuguang Wang, Robin Walters, and Robert Platt. Equivariant diffusion policy. *arXiv preprint arXiv:2407.01812*, 2024.
- [54] Jimmy Wu, Rika Antonova, Adam Kan, Marion Lepert, Andy Zeng, Shuran Song, Jeannette Bohg, Szymon Rusinkiewicz, and Thomas Funkhouser. Tidybot: Personalized robot assistance with large language models. *Autonomous Robots*, 47(8):1087–1102, 2023.
- [55] Philipp Wu, Yide Shentu, Zhongke Yi, Xingyu Lin, and Pieter Abbeel. Gello: A general, low-cost, and intuitive teleoperation framework for robot manipulators. In *2024 IEEE/RSJ International Conference on Intelligent Robots and Systems (IROS)*, pages 12156–12163. IEEE, 2024.
- [56] Xiaomeng Xu, Dominik Bauer, and Shuran Song. Robopanoptes: The all-seeing robot with whole-body dexterity. *arXiv preprint arXiv:2501.05420*, 2025.
- [57] Jingyun Yang, Zi-ang Cao, Congyue Deng, Rika Antonova, Shuran Song, and Jeannette Bohg. Equibot: Sim (3)-equivariant diffusion policy for generalizable and data efficient learning. *arXiv preprint arXiv:2407.01479*, 2024.
- [58] Yanjie Ze, Gu Zhang, Kangning Zhang, Chenyuan Hu, Muhan Wang, and Huazhe Xu. 3d diffusion policy: Generalizable visuomotor policy learning via simple 3d representations. *arXiv preprint arXiv:2403.03954*, 2024.
- [59] Tianhao Zhang, Zoe McCarthy, Owen Jow, Dennis Lee, Xi Chen, Ken Goldberg, and Pieter Abbeel. Deep imitation learning for complex manipulation tasks from virtual reality teleoperation. In *2018 IEEE international conference on robotics and automation (ICRA)*, pages 5628–5635. Ieee, 2018.
- [60] Haibo Zhao, Dian Wang, Yizhe Zhu, Xupeng Zhu, Owen Howell, Linfeng Zhao, Yaoyao Qian, Robin Walters, and Robert Platt. Hierarchical equivariant policy via frame transfer. In *Forty-second International Conference on Machine Learning*, 2025. URL <https://openreview.net/forum?id=nAv5ketrHq>.
- [61] Tony Z Zhao, Vikash Kumar, Sergey Levine, and Chelsea Finn. Learning fine-grained bimanual manipulation with low-cost hardware. *arXiv preprint arXiv:2304.13705*, 2023.
- [62] Yi Zhou, Connelly Barnes, Jingwan Lu, Jimei Yang, and Hao Li. On the Continuity of Rotation Representations in Neural Networks. In *Proceedings of the IEEE/CVF Conference on Computer Vision and Pattern Recognition*, pages 5745–5753, 2019.
- [63] Xupeng Zhu, Dian Wang, Ondrej Biza, Guanang Su, Robin Walters, and Robert Platt. Sample efficient grasp learning using equivariant models. *arXiv preprint arXiv:2202.09468*, 2022.

A Spectral Realization of the Equivariance Correction

In this section, we provide a concrete spectral realization of the equivariance correction introduced in Proposition 1, using the spherical-harmonic coefficients and Wigner D -matrices.

Proof. Let x be the observation with camera pose $R_x \in \text{SO}(3)$ and let $c_\ell(x) \in \mathbb{R}^{2\ell+1}$ denotes spherical harmonic coefficients. Under a global rotation $g \in \text{SO}(3)$ applied to both the scene and the camera, the camera pose transforms as $R_x \mapsto R_{gx} = gR_x$. Since the signal $\Phi(x)$ is expressed in the local (camera) frame, the spherical coefficients remain unchanged under the global transformation, so $c_\ell(gx) = c_\ell(x)$. Applying Equation 2 with the updated camera pose, the corrected coefficients at gx are:

$$c_{\ell,\text{corr}}(gx) = D^\ell(R_{gx}) c_\ell(gx) = D^\ell(gR_x) c_\ell(x). \quad (6)$$

Since the Wigner D -matrices D^ℓ form a group representation of $\text{SO}(3)$, they satisfy the homomorphism property: $D^\ell(gR_x) = D^\ell(g) D^\ell(R_x)$. Substituting this, we obtain:

$$c_{\ell,\text{corr}}(gx) = D^\ell(g) D^\ell(R_x) c_\ell(x) \quad (7)$$

Recognizing that $c_{\ell,\text{corr}}(x) = D^\ell(R_x) c_\ell(x)$ by Proposition 1, we conclude:

$$c_{\ell,\text{corr}}(gx) = D^\ell(g) c_{\ell,\text{corr}}(x) \quad (8)$$

Thus, the corrected coefficients $c_{\ell,\text{corr}}(x)$ transform equivariantly under the group action $g \in \text{SO}(3)$. \square

This result shows that equivariance correction can be implemented spectrally by left-multiplying the spherical harmonic coefficients with Wigner D -matrices according to the camera orientation. This aligns the signal, originally expressed in the camera frame, to a common world frame for consistent and equivariant downstream processing across varying viewpoints.

B Implementation of Our Policy

Our model consists of an $\text{SO}(3)$ -equivariant observation encoder followed by an $\text{SO}(3)$ -equivariant diffusion module, both implemented using `escnn` [3] and `e3nn` [46].

Given an observation $x \in X$, the $\text{SO}(2)$ -equivariant image encoder λ first maps the RGB image I into a regular representation, which is then mapped to a trivial representation $\lambda(I) \in \mathbb{R}^{n \times h \times w}$, where n , h , and w denote the number of channels, height, and width, respectively. These 2D features are lifted to the sphere via orthographic projection, producing a signal $\Phi(x)$ on S^2 . To account for varying viewpoints, we use the gripper orientation R_x as an *equivariance correction* factor to align the spherical signal into a common reference frame. In our setup, the wrist-mounted camera is rigidly attached to the gripper, so the gripper orientation provides a fixed proxy for the camera pose. This approximation is sufficient for aligning the image features with the proprioceptive signals, and any minor misalignments can be further handled by the equivariant convolution layers. The corrected signal is then processed by a sequence of $S^2 \rightarrow \text{SO}(3)$ and $\text{SO}(3) \rightarrow \text{SO}(3)$ spherical convolution layers to generate the signal $\Psi(x)$ on $\text{SO}(3)$. The proprioceptive state is encoded using the irreps ρ_0 and ρ_1 , and passed through $\text{SO}(3)$ -equivariant linear layers to yield Fourier coefficients of the same type as $\Psi(x)$. These are then concatenated with the image signal to form the global conditioning vector $e_o \in \mathbb{R}^{u \times d_o}$, where u is the number of channels and d_o is the feature dimension. Similarly, the noisy action chunk \mathbf{a}^k is embedded into $e_a \in \mathbb{R}^{u \times d_a \times n}$, where d_a denotes the number of action feature channels and n the number of time steps. An inverse FFT is applied to sample both e_o and e_a onto discrete subgroups, either the icosahedral group $I_{60} \subset \text{SO}(3)$ or the cyclic group $C_8 \subset \text{SO}(2)$, producing $e_o \in \mathbb{R}^{p \times d_o}$, $e_a \in \mathbb{R}^{p \times d_a \times n}$, where $p = 60$ or 8 is the number of group elements. For each group element $g \in I_{60}$ or $g \in C_8$, a shared $\text{SO}(3)$ - or $\text{SO}(2)$ -equivariant 1-D temporal U-Net processes the action sequence e_a^g , conditioned on the observation e_o^g and diffusion step k . This design follows the point-wise equivariant processing strategy proposed in [53], ensuring equivariance across group elements. Finally, an equivariant decoder maps the denoised representation to the noise estimate ϵ^k .

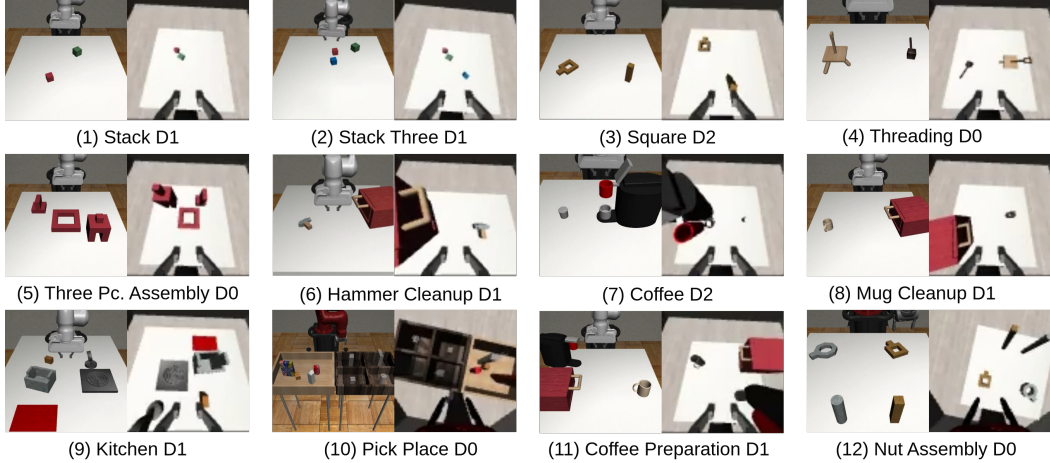


Figure 7: The twelve simulation tasks from the MimicGen [31] simulator. In each subfigure, the left image shows the task scene, while the right image shows the corresponding eye-in-hand view.

C Simulation Settings

Figure 7 illustrates the twelve tasks in the MimicGen simulation. In each subfigure, the left image shows the full environment scene from the agent’s view, while the right image is the eye-in-hand RGB observation used by the model. Following prior work [31, 53], we set the resolution of the eye-in-hand image to $3 \times 84 \times 84$ and adopt the same maximum episode length. To enable the wrist-mounted camera to capture more contextual information, we increase its FOV from 75 to 130 degrees, similar to that of a GoPro camera.

D Training Details

For the simulation experiments, we follow the hyperparameter settings from prior work [53, 5]. In detail, we use an observation window of two history steps for the $SO(3)$ version of our method, and one step for the $SO(2)$ version. In both cases, the denoising network outputs a sequence of 16 action steps, which are used for optimization during training, while only the first 8 steps are executed during evaluation. During training, input images are randomly cropped to a resolution of 76×76 , while a center crop is applied at evaluation time. We train all models using the AdamW [29] optimizer with Exponential Moving Average, and adopt the DDPM [11] framework with 100 denoising steps for both training and evaluation. For all baselines, we retain their original hyperparameter settings for evaluation and only adjust the number of training steps to ensure consistency across methods. All methods are trained on the same dataset and evaluated using three random seeds.

For the real-world experiments, we use the same hyperparameters as in the simulation, except that we replace DDPM with DDIM [44] for both training and evaluation, and reduce the number of denoising steps to 16 at evaluation time. However, we find that using a resolution of 76×76 is insufficient for fine-grained manipulation in the real world, as the extremely wide FOV from the GoPro camera causes each pixel to correspond to a relatively large spatial region in the original setting. To address this, we increase the input resolution to 224×224 . Specifically, starting from the original 720×720 RGB image captured using a GoPro with the Max Lens Mod, we apply a center crop of size 480×480 , followed by resizing to 224×224 . In addition, we apply standard data augmentations—including random cropping, random rotations, and color jitter—to improve the robustness of both our method and the baseline models.

All models are trained on single GPUs using compute clusters and workstations equipped with multiple high-performance consumer-grade GPUs.

E Simulation Full Experiment Result with Standard Error

Table 4 presents the same results as Table 1, with standard errors included.

Table 4: Maximum success rates (%) on MimicGen tasks with 100 and 200 demos across different methods, averaged over three random seeds. The \pm indicates standard error.

Method	Stack D1		Stack Three D1		Square D2		Threading D0	
	100	200	100	200	100	200	100	200
Ours(SO(3))	99.3 \pm 1.2	100.0 \pm 0.0	70.0 \pm 2.0	88.0 \pm 2.0	34.7 \pm 4.2	51.3 \pm 2.3	90.0 \pm 2.0	92.0 \pm 0.0
Ours(SO(2))	98.0 \pm 2.0	100.0 \pm 0.0	74.7 \pm 7.6	88.0 \pm 2.0	32.0 \pm 0.0	50.7 \pm 5.0	84.7 \pm 1.2	87.3 \pm 3.1
DiffPo	90.7 \pm 4.2	96.0 \pm 2.0	43.3 \pm 4.2	76.7 \pm 4.2	12.0 \pm 2.0	25.3 \pm 3.1	77.3 \pm 10.3	86.7 \pm 7.0
EquiDiff	96.0 \pm 0.0	98.7 \pm 1.2	61.3 \pm 5.0	80.0 \pm 2.0	8.7 \pm 1.2	19.3 \pm 1.2	88.7 \pm 5.8	92.0 \pm 2.0
ACT	45.3 \pm 7.6	77.3 \pm 2.3	12.0 \pm 2.0	36.7 \pm 9.9	2.7 \pm 1.2	10.0 \pm 2.0	36.0 \pm 6.9	53.3 \pm 6.1

Method	Three Pc. Assembly D0		Hammer Cleanup D1		Mug Cleanup D1		Coffee D2	
	100	200	100	200	100	200	100	200
Ours(SO(3))	70.7 \pm 1.15	79.3 \pm 1.15	66.0 \pm 0.00	73.3 \pm 1.15	54.0 \pm 8.7	58.7 \pm 2.3	64.0 \pm 0.0	68.7 \pm 3.1
Ours(SO(2))	74.7 \pm 1.15	80.0 \pm 2.00	70.7 \pm 1.15	73.3 \pm 2.31	56.0 \pm 2.0	60.7 \pm 1.2	58.7 \pm 3.1	63.3 \pm 4.2
DiffPo	72.7 \pm 3.06	73.3 \pm 2.31	58.7 \pm 7.57	63.3 \pm 11.72	49.3 \pm 8.3	61.0 \pm 1.7	53.3 \pm 3.1	54.7 \pm 4.2
EquiDiff	74.0 \pm 5.29	78.7 \pm 1.15	59.3 \pm 4.16	74.0 \pm 2.00	50.7 \pm 2.3	62.0 \pm 0.0	47.3 \pm 3.1	61.3 \pm 2.3
ACT	28.0 \pm 4.00	50.0 \pm 5.29	34.7 \pm 2.31	62.7 \pm 5.77	24.7 \pm 3.1	37.3 \pm 5.8	20.7 \pm 3.1	34.7 \pm 2.3

Method	Kitchen D1		Pick Place D0		Coffee Preparation D1		Nut Assembly D0	
	100	200	100	200	100	200	100	200
Ours(SO(3))	75.3 \pm 3.1	79.3 \pm 4.2	42.0 \pm 4.4	65.7 \pm 5.5	40.7 \pm 2.3	61.3 \pm 2.3	75.3 \pm 2.5	82.0 \pm 7.5
Ours(SO(2))	64.7 \pm 2.3	72.0 \pm 2.0	45.7 \pm 8.0	61.0 \pm 5.6	46.7 \pm 4.6	56.0 \pm 0.0	73.7 \pm 7.6	84.3 \pm 1.5
DiffPo	60.7 \pm 8.1	70.7 \pm 3.1	36.3 \pm 2.1	47.7 \pm 1.5	37.3 \pm 1.2	52.0 \pm 5.3	51.3 \pm 3.8	62.3 \pm 1.5
EquiDiff	55.3 \pm 1.2	66.7 \pm 2.3	27.7 \pm 2.9	46.3 \pm 3.5	27.3 \pm 1.2	38.7 \pm 2.3	40.0 \pm 4.0	56.3 \pm 3.1
ACT	21.3 \pm 1.2	50.7 \pm 3.1	8.7 \pm 1.5	13.7 \pm 2.5	7.3 \pm 2.3	16.0 \pm 2.0	36.7 \pm 1.2	49.0 \pm 2.0

F The Benefits of Pretraining

While our method already benefits from explicit equivariance, we further investigate whether incorporating a pretrained image encoder can enhance performance. Intuitively, pretraining introduces stronger geometric priors and improves feature quality, especially beneficial in data-limited settings.

To evaluate this, we conduct experiments on five tasks from the MimicGen [31] using 100 demons. We compare the SO(2) version of our method (Ours) and the original Diffusion Policy (DP), each with two variations: *Pretraining* (pretrain the equivariant ResNet-18 for ours and the standard ResNet-18 for DP on ImageNet-1k [39]) and *Scratch* (train the image encoders from scratch). Figure 8 shows the learning curves comparing evaluation success rates versus training epochs, and Table 5 shows the maximum evaluation success rate. We can conclude that pretraining improves learning speed and final performance for both methods compared to random initialization. However, the pretrained equivariant encoder achieves a 13.3% improvement, exceeding the 8.2% achieved by Diffusion Policy. This suggests that symmetry-aware pretraining provides more effective representations. Moreover, even with a pretrained image encoder, Diffusion Policy still underperforms compared to our method trained from scratch, further highlighting the strength of our model design.

G Details of the Real-World Experiment

Figure 9 shows our real-world experimental setup. Demonstrations are collected using the Gello teleoperation interface [55]. While the robot is teleoperated in joint space, we record end-effector actions, including position, rotation, and gripper state. Visual observations and actions are recorded synchronously at each timestep.

Figure 10 illustrates the initial state distributions for each task. In *Box-Pipe Disassembly*, two pipes with different colors are connected to a junction box, where one pipe shares the same color as the box may confuse the policy. The orientations of the pipes are randomized. In *U-Pipe Disassembly*, four

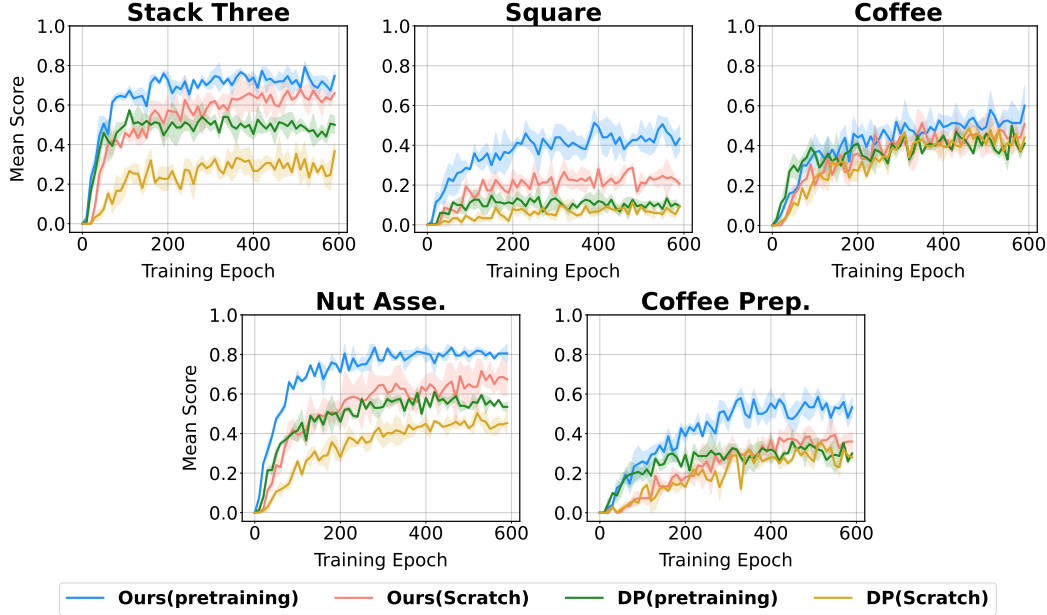


Figure 8: Learning curves of our methods and Diffusion Policy. With pretraining, our method generally converges faster and achieves higher final performance.

Table 5: A subset of the twelve simulation tasks is used to compare the performance of using a pretrained image encoder versus training from scratch. Results are averaged over three random seeds. We use the SO(2) version of our method for this comparison. Values in parentheses indicate the performance difference between the pretrained and scratch settings.

Method	Mean	Coffee	Square	Stack Three	Nut Assembly	Coffee Preparation
Ours (Pretraining)	70.5(+13.3)	66.7 (+8.0)	56.0 (+24.0)	81.3 (+6.6)	85.0 (+11.3)	63.3 (+16.6)
Ours (Scratch)	57.2	58.7	32.0	74.7	73.7	46.7
DP (Pretraining)	47.6(+8.2)	51.3 (-2.0)	18.7 (+6.7)	61.3 (+18.0)	62.7(+11.4)	44.0 (+6.7)
DP (Scratch)	39.4	53.3	12.0	43.3	51.3	37.3

pipe fittings are arranged in a U-shape and initialized with random rotations. In *3D-Pipe Disassembly*, two pipes are connected with independently randomized 3D orientations. In *Grocery Bag Retrieval*, a toy banana is randomly placed inside a deformable plastic bag. The robot must reach into the bag, identify and retrieve the banana, and place it into a transparent container with minor positional variation. All subfigures in Figure 10 show averaged visualizations across multiple randomized initializations.

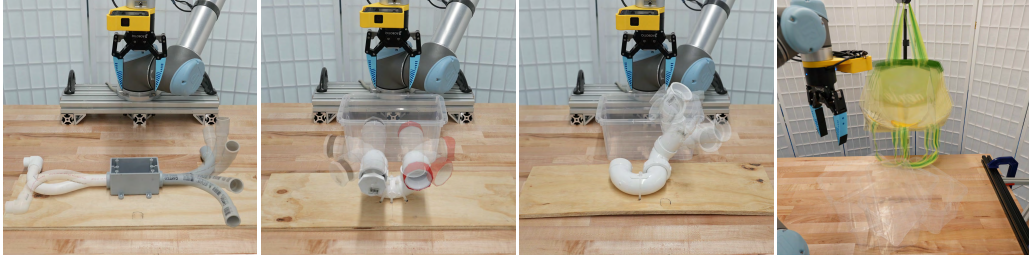
We visualize one episode for each task in Figure 11. These tasks emphasize different aspects. The pipe disassembly tasks require precise, closed-loop control to smoothly extract the pipes, which is challenging for open-loop policies. The Grocery Bag Retrieval task highlights the importance of the eye-in-hand camera, as the target object is difficult to perceive and localize using only external views.

H Real World Experiment Failure Analysis

In the *Box-Pipe Disassembly* task, one of the primary failure cases arises from the inability to distinguish between the gray junction box and the gray pipe. For the original Diffusion Policy, the policy consistently misidentifies the box as the pipe to be disassembled, which triggers the robot’s emergency stop. While our method occasionally encounters the same issue, the failure rate is significantly lower. This suggests that our method is more data-efficient and better at learning robust visual distinctions from limited demonstrations.



Figure 9: Real-world experimental setup. We use a UR5 robot equipped with a Robotiq-85 gripper and custom-designed soft fingers. A GoPro camera is mounted on the wrist to capture visual observations. Demonstrations are collected using the Gello teleoperation interface (bottom right).



(a) Box-Pipe Disassembly (b) U-Pipe Disassembly (c) 3D-Pipe Disassembly (d) Grocery Bag Retrieval

Figure 10: Distribution of random initial states used in the real-world experiments.

In the *U-Pipe Disassembly* task, a common failure mode for our method and the baseline occurs when pulling the red pipe inadvertently causes a connected pipe to be extracted as well. In such cases, the robot grasps both pipes simultaneously. We consider this a partial success. However, the baseline additionally suffers from incorrect orientation predictions under certain initial states, leading to more frequent failures.

In the *3D-Pipe Disassembly* task, our method occasionally fails to identify the correct grasp orientation. In contrast, the baseline struggles consistently with this issue and rarely completes the task successfully. One major contributing factor is the multimodality of the task. During data collection, it is difficult to maintain consistency in demonstration strategies because pipes can be grasped in multiple orientations. Nevertheless, by incorporating 3D symmetries, our method is more robust to such variations and generalizes better across diverse configurations.

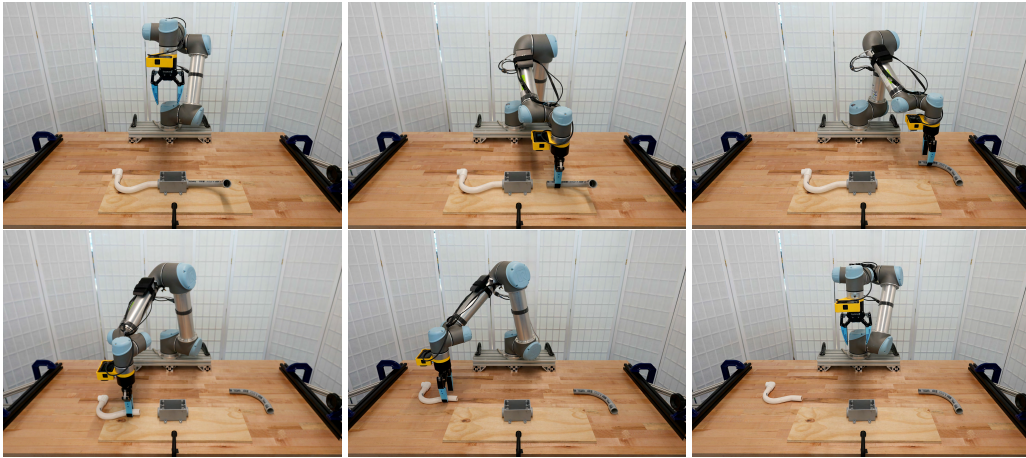
In the *Grocery Bag Retrieval* task, failure cases primarily result from unsuccessful grasp attempts or inaccuracies during the placement phase. The deformable nature of the bag and the partial occlusion of the banana present additional challenges, especially under limited visual feedback.

I Broader Impact

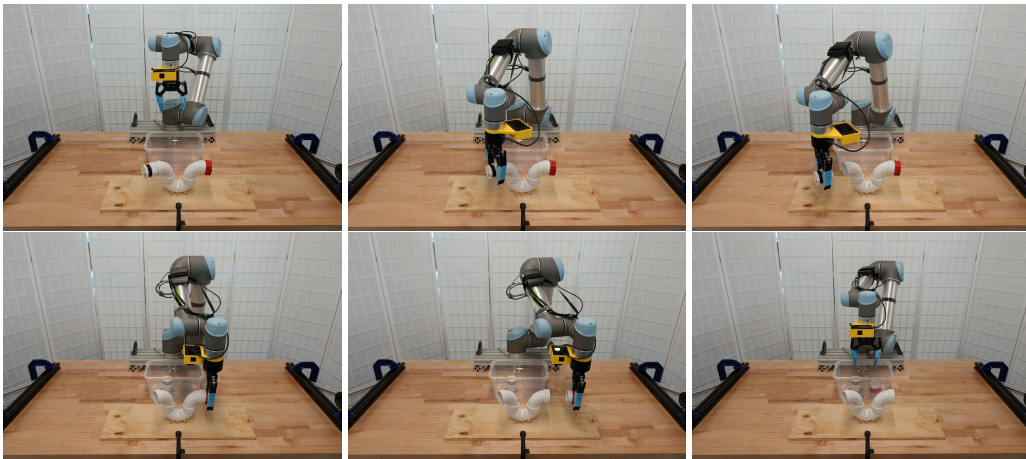
This work has several potential social impacts, both positive and negative. On the positive side, our proposed method enables more data-efficient and generalizable robot policy learning in 3D

environments. This can facilitate the development of more robust and capable household robots, particularly in settings where labeled demonstrations are limited. Moreover, by leveraging geometric symmetries and closed-loop visuomotor control from wrist-mounted cameras, our method could lower the barrier for deploying autonomous robots in unstructured real-world environments, thereby expanding accessibility and utility.

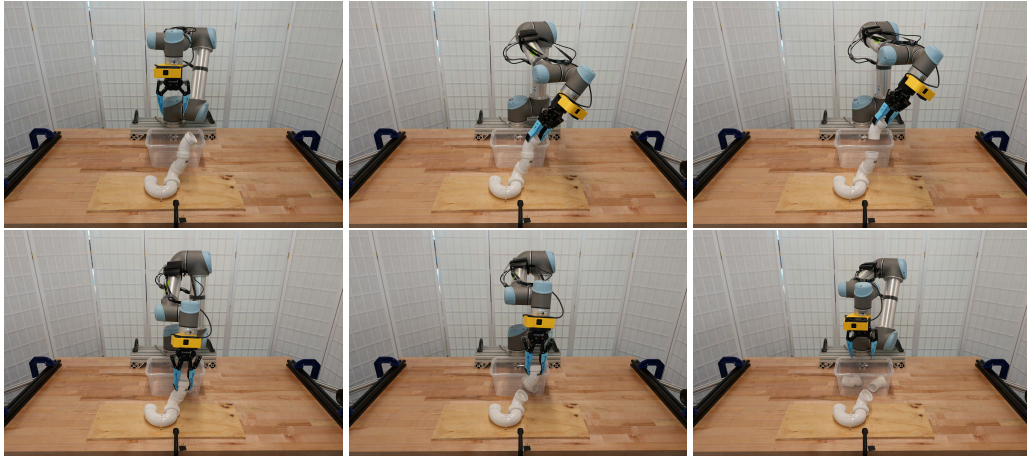
However, as with many data-driven learning methods, our approach inherits limitations tied to the quality and intent of the training data. Since the robot policy is learned entirely through imitation, any unsafe, biased, or suboptimal behavior demonstrated during data collection may be reflected in the final policy. Furthermore, the increased autonomy enabled by our method underscores the importance of safety monitoring and responsible deployment, especially in applications involving human interaction.



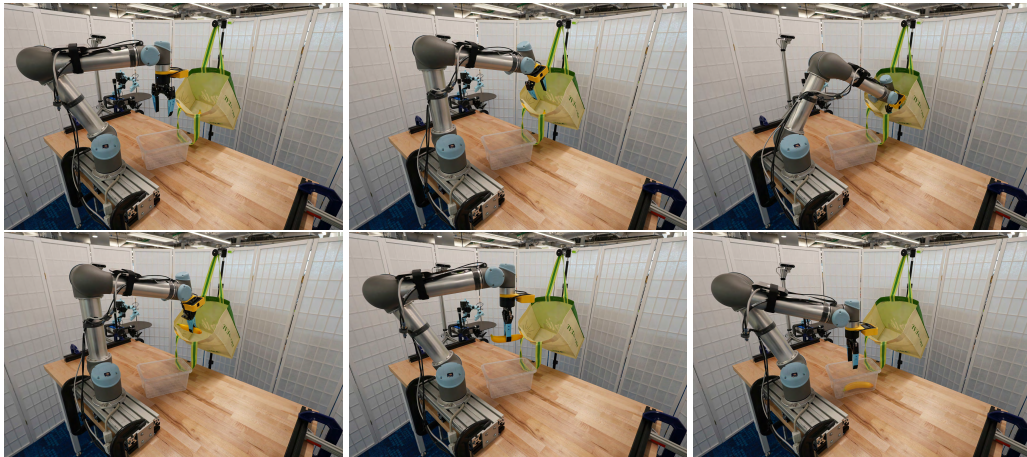
(a) Box-Pipe Disassembly



(b) U-pipe Disassembly



(c) 3D-Pipe Disassembly



(d) Grocery Bag Retrieval

Figure 11: Visualization of one episode for each task. Each subfigure illustrates the trajectory of key action steps.